ARTICLE IN PRESS

Materials Today Physics xxx (xxxx) xxx

Contents lists available at ScienceDirect

Materials Today Physics

journal homepage: www.journals.elsevier.com/materials-today-physics

Magnetotransport properties of ternary tetradymite films with high mobility

Patrick J. Taylor [a,**], Brandi L. Wooten [b], Owen A. Vail [a], Harry Hier [a], Joseph P. Heremans [b,c,d,***], Jagadeesh S. Moodera [e,f,****], Hang Chi [g,h,*]

[a] DEVCOM Army Research Laboratory, Adelphi, MD, 20783, USA
[b] Department of Materials Science and Engineering, The Ohio State University, Columbus, OH, 43210, USA
[c] Department of Mechanical and Aerospace Engineering, The Ohio State University, Columbus, OH, 43210, USA
[d] Department of Physics, The Ohio State University, Columbus, OH, 43210, USA
[e] Francis Bitter Magnet Laboratory, Plasma Science and Fusion Center, Massachusetts Institute of Technology, Cambridge, MA, 02139, USA
[f] Department of Physics, Massachusetts Institute of Technology, Cambridge, MA, 02139, USA
[g] Department of Physics, University of Ottawa, Ottawa, ON, K1N 6N5, Canada
[h] Nexus for Quantum Technologies, University of Ottawa, Ottawa, ON, K1N 6N5, Canada

ARTICLE INFO

Keywords:
Tetradymites
Molecular beam epitaxy
Quantum oscillation
Fermi surface

ABSTRACT

$(Bi,Sb)_2(Te,Se)_3$ tetradymite materials are among the most efficient for thermoelectric energy conversion, and most robust for topological insulator spintronic technologies, but should possess rather disparate doping properties to be useful for either technology. In this work, we report results on the molecular beam epitaxy growth of *p*-type $(Bi_{0.43}Sb_{0.57})_2Te_3$ and *n*-type $Bi_2(Te_{0.95}Se_{0.05})_3$ that can contribute to both technology bases, but are especially useful for topological insulators where low bulk doping is critical for devices to leverage the Dirac-like topological surface states. Comprehensive temperature, field and angular dependent magnetotransport measurements have attested to the superior quality of these ternary tetradymite films, displaying low carrier density on the order of 10^{18} cm^{-3} and a record high mobility exceeding 10^4 cm^2 V^{-1} s^{-1} at 2 K. The remarkable manifestation of strong Shubnikov–de Haas (SdH) quantum oscillation under 9 T at liquid helium temperatures, as well as the analyses therein, has allowed direct experimental investigation of the tetradymite electronic structure with optimized ternary alloying ratio. Our effort substantiates tetradymites as a critical platform for miniaturized thermoelectric cooling and power generation in wearable consumer electronics, as well as for futuristic topological spintronics with unprecedented magnetoelectric functionalities.

1. Introduction

Research effort in tetradymites date back to the report from Goldsmid and Douglas who identified Bi_2Te_3 as a viable option for all-solid-state thermoelectric refrigeration [1]. Subsequent research yielded *p*-type and *n*-type solid solutions in the $(Bi,Sb)_2(Te,Se)_3$ family as the most successful thermoelectrics suitable for commercialization at room to low temperatures [2,3]. These $(Bi,Sb)_2(Te,Se)_3$-based materials since have successfully breached the challenging figure of merit $zT = 1$ threshold which remains as an important materials-quality benchmark [4–8]. The interest in epitaxial films was driven when Hicks and Dresselhaus calculated that quantum confinement may significantly boost zT [9,10], and as a result [11], several initiatives explored the growth of novel epitaxial superlattices [12–14].

Because of the strong spin-orbit coupling associated with the large atomic number elements, tetradymites were theoretically proposed [15] and experimentally demonstrated [16–18] as archetypical three-dimensional (3D) topological insulators, featuring Dirac-like linearly dispersed helical surface states. This has presaged a vast array of new topologically nontrivial materials showcasing novel phenomena

* Corresponding authors.
** Corresponding author. DEVCOM Army Research Laboratory, Adelphi, MD, 20783, USA
*** Corresponding authors.
**** Corresponding author.
E-mail addresses: patrick.j.taylor36.civ@army.mil (P.J. Taylor), heremans.1@osu.edu (J.P. Heremans), moodera@mit.edu (J.S. Moodera), hang.chi@uottawa.ca (H. Chi).

https://doi.org/10.1016/j.mtphys.2024.101486
Received 14 May 2024; Received in revised form 10 June 2024; Accepted 17 June 2024
Available online 18 June 2024

[19–25]. And even though epitaxial tetradymite films have enabled new discoveries such as the quantum anomalous Hall effect [26–28] as well as breaking the time-reversal symmetry via proximitized exchange coupling [29–31], the quality of epitaxial $(Bi,Sb)_2(Te,Se)_3$ materials for topological applications is generally lower than their equivalent counterpart grown from the melt in bulk form. The lower quality for epitaxial films is generally believed to derive from the non-equilibrium growth mode inherent in molecular beam epitaxy (MBE) that yields films replete with point defects that can cause unintended doping and scattering, as well as extended crystallographic defects from antiphase domains with localized rotational disorder [8].

In this work, we report results from a new strategy that more closely approaches equilibrium growth conditions using state-of-the-art MBE method, where the carrier type and concentration are controlled by the composition only, without employing extrinsic doping. The temperature, field, as well as angular dependences of the magnetotransport parameters in *p*-type $(Bi_{0.43}Sb_{0.57})_2Te_3$ (BAT, thickness $t = 220$ nm) and *n*-type $Bi_2(Te_{0.95}Se_{0.05})_3$ (BTS, $t = 150$ nm) films are thoroughly investigated. This strategy enables unusually high mobility in this work, which leads to robust Shubnikov–de Haas (SdH) quantum oscillations in a wide range of temperature in various field orientations. These efforts allow for in-depth understanding of the Fermi pockets of these tetradymite thin films.

2. Methods

The growth of tetradymite thin films were carried out in a modular Gen II MBE system with a base pressure of 10^{-8} Pa, and from conventional Knudsen-style cells using 99.999% pure source materials. Quarters of full three-inch semi-insulating GaAs(001) wafers were used to facilitate unambiguous interpretation of thermal- and magneto-transport data. MBE is an inherently non-equilibrium, metastable growth process so the two-fold strategy adopted for this work is intended to converge towards more equilibrium processes: 1. employ a 595 K substrate temperature and 2. invoke a VI/V ratio of 60 for group VI elements (Te and Se) to group V elements (Bi and Sb). The single crystalline nature of the *c*-oriented as-grown films was confirmed using *in situ* reflection high-energy electron diffraction (RHEED) and *ex situ* X-ray diffraction (XRD) techniques (see Supplementary Fig. 1). The compositional dependence was systematically determined by several techniques. For the *n*-type compositions of BTS, leveraging the substantial difference in the lattice constants, high resolution XRD was used to calculate the *c*-axis lattice constant and the composition. For *p*-type compositions, energy-dispersive X-ray spectroscopy (EDS) was applied within transmission electron microscope (TEM) to calibrate the full range of BAT. The compositions reported here were found to yield the lowest carrier density and highest mobility. *In situ* angle-resolved photoemission spectroscopy (ARPES) was carried out to capture the energy-momentum dispersion along the Γ-K high symmetry lines of the Brillouin zone.

Temperature and magnetic field dependent transport measurements were performed in the temperature range of 1.8–300 K in a Quantum Design Physical Property Measurement System (PPMS) equipped with a 9 T superconducting magnet. An ac electric current (I_x) with a typical magnitude of 5 μA was injected into the current channel of a 10 × 30 μm^2 Hall bar residing in the crystallographic *a*-*b* plane, while longitudinal (V_x) and transverse (V_y) voltages were simultaneously monitored using a lock-in technique (Stanford Research SR830). For aligning the magnetic field **B**, a horizontal rotator was used with an angular resolution of ~0.1°. Thermoelectric measurements of cleaved as-grown samples (3.5 × 4.0 mm^2 for BAT and 3.5 × 6.0 mm^2 for BTS, respectively) were taken in a standard liquid N_2 cryostat using a conventional steady state technique. Absolute copper-constantan thermocouples were fixed at two points along the sample length to measure the temperature difference in the direction of heat flow; the copper legs of these thermocouples were also used to measure the Seebeck voltage. Current wires were added to perform conductivity measurements.

3. Results and discussion

As shown in Fig. 1a, in the absence of external magnetic field *B*, the longitudinal electrical resistivity $\rho_{xx}(T)$ of both *p*-type BAT and *n*-type BTS display a metallic behavior with positive temperature coefficient for $2\ K \le T \le 300\ K$. The residual resistance ratio [$RRR \equiv \rho_{xx}(300\ K)/\rho_{xx}(2\ K)$] is 14 and 16 for BAT [$\rho_{xx}(2\ K) = 0.27$ mΩ cm] and BTS [$\rho_{xx}(2\ K) = 0.10$ mΩ cm], respectively. The dominant carrier type is consistent with the Seebeck coefficient in Fig. 1b (left axis, where the right axis illustrates the thermoelectric power factor $PF \equiv S^2/\rho_{xx}$), as well as the band dispersion revealed by ARPES (Fig. 2a and d) [8,32]. Near room temperature, the slope of $\rho_{xx}(T)$ flattens, forming a peak due to the bipolar effect, well known for tetradymites when the minority carriers are thermally activated and contribute to charge transport [33,34]. When subjected to $B = 9$ T, ρ_{xx} increases in the entire measured *T* range for both BAT and BTS, while maintaining the metallicity. The sizable magnetoresistance (MR, see also Fig. 2b and e) is a synergy of both the low carrier density *n* (~10^{18} cm^{-3}, Fig. 1c) and, to the best of our knowledge, the record high mobility *μ* (>10^4 $cm^2\ V^{-1}\ s^{-1}$ at 2 K, Fig. 1d) in these optimally grown ternary tetradymite films. The solid symbols in Fig. 1c and d represent the Hall carrier density n_{Hall} [$\equiv 1/qR_H$, $q = e$ (–*e*) for hole (electron), with *e* the elementary charge] and the Hall mobility

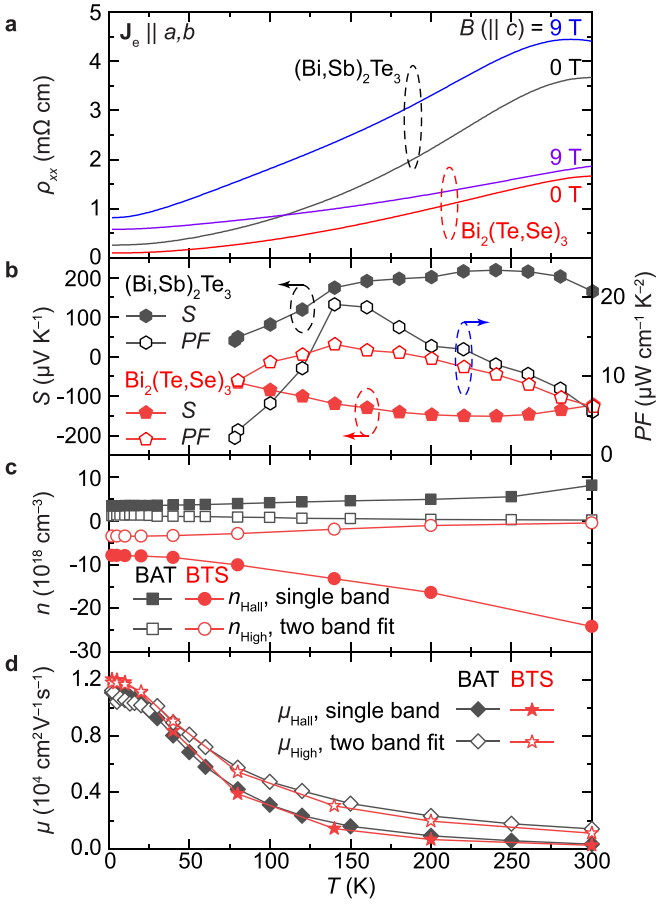

Fig. 1. | Temperature dependence of the transport properties. a Temperature dependent longitudinal electrical resistivity $\rho_{xx}(T)$ of *p*-type $(Bi,Sb)_2Te_3$ (BAT, black line at 0 T) and *n*-type $Bi_2(Te,Se)_3$ (BTS, red line at 0 T), with as-grown Seebeck coefficient *S* and power factor $PF \equiv S^2/\rho_{xx}$ in **b**. At applied magnetic field $B = 9$ T, large magnetoresistance is evident for BAT (blue line) and BTS (purple line), resulting from (**c**) low carrier density *n* (~10^{18} cm^{-3}, positive/negative values for hole/electron-type carriers) and (**d**) high mobility *μ* exceeding 10^4 $cm^2\ V^{-1}\ s^{-1}$ at 2 K. In view of the bulk dominated nature of the transport, both single-band model (solid symbols) and two-band fitting (open symbols) have been used to estimate the transport parameters.

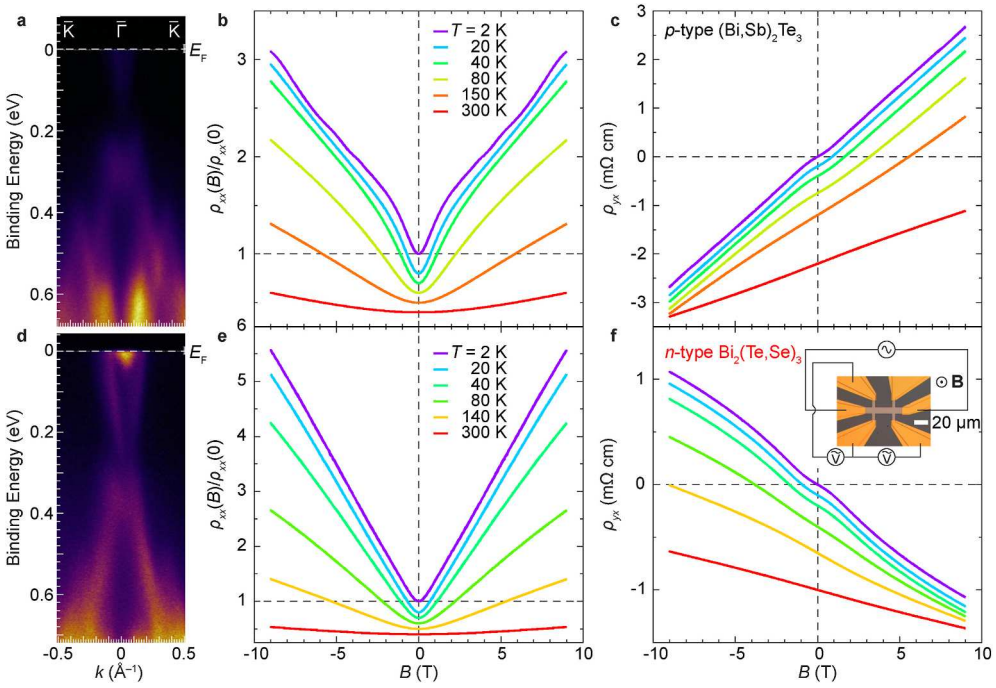

Fig. 2. | Magnetic field dependent longitudinal and Hall resistivity. ARPES (**a**,**d**), magnetic field dependence of magnetoresistance (MR) $\rho_{xx}(B)/\rho_{xx}(0)$ (**b**,**e**) and Hall resistivity $\rho_{yx}(B)$ (**c**,**f**) at selected few temperatures, for *p*-type $(Bi,Sb)_2Te_3$ (**a**–**c**) and *n*-type $Bi_2(Te,Se)_3$ (**d**–**f**), respectively. Inset in **f**, optical microscopic image of a typical e-beam lithography Hall bar. The curves (**b**,**c**,e,**f**) are vertically shifted for clarity. The *p*-type film manifests Shubnikov–de Haas (SdH) quantum oscillations in ρ_{xx} at low T (**b**), while the *n*-type sample develops a large quasi-linear MR without discernible SdH feature at the lowest measured $T = 2$ K under out-of-plane B up to 9 T (**e**). The nonlinearity in $\rho_{yx}(B)$ (**c**,**f**) suggests multi-carrier transport.

μ_{Hall} [$\equiv|R_H|/\rho_{xx}(B=0)$], respectively, where the Hall coefficient R_H is estimated, presuming a single band, from the linear slope of the low field Hall resistivity $\rho_{yx}(B)$ in Fig. 2 (see also Supplementary Fig. 2). Towards 300 K, the aforementioned bipolar mechanism leads to reduced magnitude of R_H, owing to the contribution from minority carriers with the opposite sign. The resultant artificial uprising of the magnitude of n_{Hall} at higher T hence reveals the limitation of the oversimplified single-band framework.

Nonlinearity develops in $\rho_{yx}(B)$ with decreasing T for both BAT (Fig. 2c) and BTS (Fig. 2f). Together with the observation that Kohler's plot of $\Delta\rho_{xx}(B)/\rho_{xx}(0)$ deviates from a single scaling functional $f(B/\rho_{xx}(0))$ in Supplementary Fig. 3, it suggests the existence of multiple carriers with different Hall mobility (effective mass or scattering time τ_S). In order to decipher contributions from different bands, conductivity tensor $\sigma_{xy} = \rho_{yx}/\left(\rho_{xx}^2+\rho_{yx}^2\right)$ and $\sigma_{xx} = \rho_{xx}/\left(\rho_{xx}^2+\rho_{yx}^2\right)$ are examined against a two-band model [35],

$$\sigma_{xy} = n_H e\mu_H^2 B\left[\frac{1}{1+(\mu_H B)^2}+C_{xy}\right], \quad (1)$$

and

$$\sigma_{xx} = ne\mu\left[\frac{1}{1+(\mu B)^2}+C_{xx}\right]. \quad (2)$$

Here n_H (n) and μ_H (μ) denote the carrier density and mobility from the high-mobility dominant band as estimated using σ_{xy} (σ_{xx}), while C_{xy} (C_{xx}) refers to the contribution from the less-mobile secondary pockets. As demonstrated in Supplementary Fig. 4, the two-band model fits reasonably well the experimental data measured in a wide range of B and T for both BAT and BTS. The model of Eq. (1) may be further improved (see the insets of Supplementary Figs. 4a and 4b) by explicitly considering the B dependence originated from the secondary carriers [36,37],

$$\sigma_{xy} = \frac{n_H e\mu_H^2 B}{1+(\mu_H B)^2}+\frac{n_L e\mu_L^2 B}{1+(\mu_L B)^2}, \quad (3)$$

where the secondary carrier density n_L and mobility μ_L are introduced as the new fitting parameters replacing C_{xy}. The transport parameters of the dominant band determined via the two-band model are plotted in Fig. 1c and d (open symbols), where $n_H = 1.1 \times 10^{18}$ cm^{-3} and -3.6×10^{18} cm^{-3} at $T = 2$ K for BAT and BTS, respectively.

The manifestation of nonlinear $\rho_{yx}(B)$ is accompanied by MR evolving from parabolic shape towards quasi-linear dependence upon cooling (Fig. 2b and e). A MR value [$\equiv(\rho_{xx}(9\text{ T})/\rho_{xx}(0)-1)\times 100\%$] exceeding 200% (450%) for BAT (BTS) has been observed at $T = 2$ K. This impressive MR likely originates from the dominant carrier with an extremely high mobility, whose filed dependence is well characterized by the two-band model (Supplementary Fig. 4d) [35,38–41]. It is remarkable that robust SdH quantum oscillations emerge in ρ_{xx} for BAT at low T with out-of-plane B (and for other configurations in Supplementary Figs. 5 and 6). For BTS, SdH signals are also discernible with in-plane perpendicular B (Supplementary Figs. 7 and 8), although no oscillations were detected under the out-of-plane Hall configuration up to 9 T. The appearance of SdH oscillations at liquid helium T under modest B attests to the superior quality of these ternary tetradymite films.

We now turn to the SdH behavior of BAT, whose detailed B, T and angular θ (inset of Fig. 4a) dependences are instrumental in experimentally probing the Fermi surface (FS) morphology. As illustrated in Fig. 3a, the oscillatory $\Delta\rho_{xx}(B)/\rho_{xx}(0)$, after removing a smooth background, displays periodic-like profile against $1/B$, which can be described by the Lifshitz–Kosevich (LK) theory [42],

$$\Delta\rho_{xx}(B)\Big/\rho_{xx}(0) = a\left(\frac{B}{F}\right)^{1/2} R_T R_D \cos\left[2\pi\left(\frac{F}{B}+\gamma-\delta\right)\right]. \quad (4)$$

Here a is the amplitude constant, F is the oscillation period, phase factors

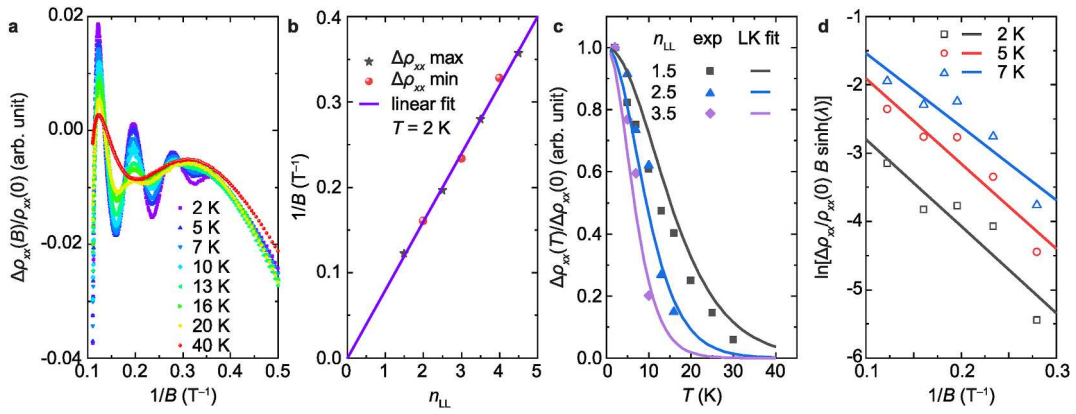

Fig. 3. | Quantum oscillation in *p*-type $(Bi,Sb)_2Te_3$. **a** After subtracting a smooth background, traces of $\Delta\rho_{xx}(B)/\rho_{xx}(0)$ vs. $1/B$ at selected T reveal Shubnikov–de Haas (SdH) quantum oscillations. **b** Landau level index plot of $\Delta\rho_{xx}$ extrema vs. n_{LL}. The linear fit points to $n_0 = 0.02$, suggesting a Berry curvature of 0, consistent with bulk dominated transport. **c** Temperature damping of the SdH oscillation amplitudes, which are well characterized by Lifshitz–Kosevich (LK) formula with an effective mass 0.079(±0.014) m_e. **d** Dingle plots of $\ln[\Delta\rho_{xx}/\rho_{xx}(0)\ B\ \sinh(\lambda)]$ vs. $1/B$ at selected T, which has been used to estimate the phase coherence lifetime $\tau \sim 1.2 \times 10^{-13}$ s.

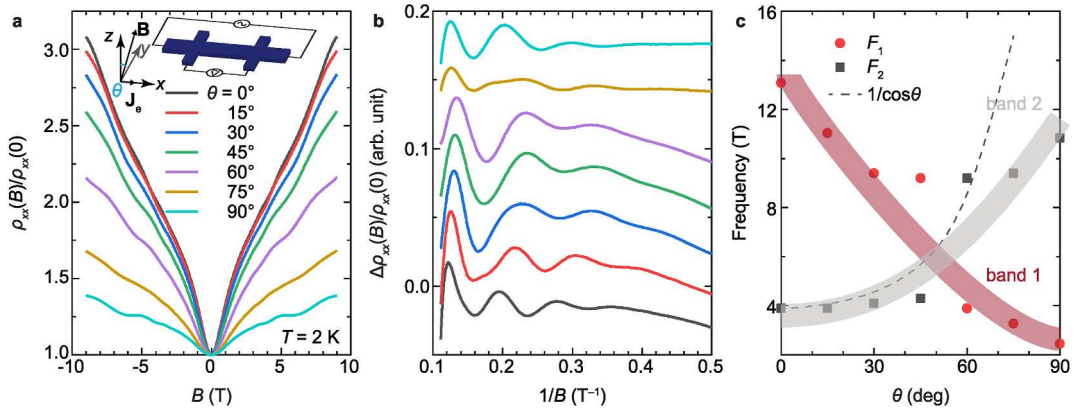

Fig. 4. | Angular dependence of the quantum oscillation. **a** Magnetoresistance measured at selected angles θ with respect to the film normal direction, as depicted in the inset, where $\theta = 0°$ indicates out-of-plane magnetic field **B** and $\theta = 90°$ corresponds to **B** parallel to current $\mathbf{J}_e$. **b** Oscillatory traces of $\Delta\rho_{xx}(B)/\rho_{xx}(0)$ vs. $1/B$ (shifted vertically for clarity). **c** Fast Fourier transform frequency analysis of the SdH spectra, revealing contributions from two 3D bulk pockets. The dashed line of $1/\cos\theta$ indicates that the secondary band 2 is not of 2D origin.

$\delta = 0$ ($\pm 1/8$) for 2D (3D) FS and $\gamma = 1/2 - \phi_B/(2\pi)$ with φ_B the Berry phase. The temperature and Dingle factors are given by

$$R_T = \lambda(T) / \sinh(\lambda(T)), \tag{5}$$

and

$$R_D = \exp(-\lambda(T_D)), \tag{6}$$

using the expression

$$\lambda(T) = \frac{2\pi^2 k_B m^*_{cyc} T}{\hbar e B}, \tag{7}$$

where k_B, m^*_{cyc} and ħ are the Boltzmann constant, the cyclotron effective mass and the reduced Planck constant, respectively. The Dingle temperature is governed by scattering via $T_D = \hbar/(2\pi k_B \tau)$, where τ is the phase coherence lifetime of the carriers. The Landau fan diagram has been constructed at $T = 2$ K in Fig. 3b for the dominant carrier by assigning SdH $\Delta\rho_{xx}$ minima [43] as integer Landau level (LL) indices n_{LL}. Extrapolation to $1/B = 0$ leads to $n_0 = 0.02$, based on which φ_B is determined to be close to 0, consistent with 3D bulk metallic behavior with insignificant topological surface transport [44]. The slope yields the dominant SdH frequency $F = 12.4$ T, with Fermi wave vector $k_F = \sqrt{2eF/\hbar} = 0.019$ Å^{-1}. By taking into account both the spin ($N_s = 2$) and valley ($N_v = 6$) degeneracies [8,45–49], the SdH carrier density $n_{SdH} = N_s N_v k_F^3/(6\pi^2) = 1.4 \times 10^{18}$ cm^{-3} is in excellent agreement with n_H of 1.1×10^{18} cm^{-3} extracted from the two-band modeling for the high-mobility dominant band. As shown in Fig. 3c and d, the T and B dependence of the SdH oscillation amplitudes reveal $m^*_{cyc} = 0.079\ m_e$ (m_e being the rest mass of free electron) with $\tau \sim 1.2 \times 10^{-13}$ s, consistent with typical tetradymites. As usual, the SdH mobility derived using the phase coherence lifetime $\mu_{SdH} = e\tau/m^*_{cyc} = 2.7 \times 10^3$ cm^2 V^{-1} s^{-1} at 2 K, is smaller than the Hall mobility estimated directly from transport, which involves the scattering time, the average time between momentum-altering scattering events.

Fig. 4a depicts the SdH signals at various θ, where B is tilted from the out-of-plane orientation ($\theta = 0°$) to that of the in-plane electric current density J_e ($\theta = 90°$). The oscillatory $\Delta\rho_{xx}(B)/\rho_{xx}(0)$ traces plotted against $1/B$ (Fig. 4b) and its out-of-plane component $1/B_\perp$ (Supplementary Fig. 5a) suggest that the angular dependence is incompatible with a 2D FS that leads to a $1/\cos\theta$ dependence (dashed line in Fig. 4c). This confirms the 3D nature of the pockets responsible for the SdH oscillations. Apart from the dominant F_1 from the high-mobility band, fast Fourier transform (FFT) analysis indeed further corroborates the coexistence of an additional frequency F_2 (Supplementary Fig. 5b) with somewhat smaller m^*_{cyc} of 0.067 m_e (Supplementary Fig. 6). The θ dependence of F_1 and F_2 are visualized in Fig. 4c, providing experimental assessment of the FS

morphology in ternary tetradymites.

4. Conclusion

In summary, we have grown ternary tetradymite thin films that host low $n \sim 10^{18}$ cm^{-3} and exhibit a record high μ exceeding 10^4 cm^2 V^{-1} s^{-1} at 2 K for both *p*-type BAT and *n*-type BTS. The *T*, *B* and θ dependent magnetotransport experiments and subsequent in-depth SdH analyses have disclosed contributions from relevant bulk bands near the Fermi level. The present study has carefully examined the bulk electronic band structure with optimized ternary alloying ratio, a regime that is of strong technological interest serving as a fertile playground for miniature thermoelectric modules compatible with commercial wearable electronics [50], as well as for materializing futuristic spintronic and topological devices [51], especially when quantized Hall channels associated with topological surface conduction are made to prevail with reduced film thickness.

CRediT authorship contribution statement

Patrick J. Taylor: Writing – original draft, Investigation, Funding acquisition, Conceptualization. **Brandi L. Wooten:** Writing – review & editing, Investigation. **Owen A. Vail:** Writing – review & editing, Investigation. **Harry Hier:** Writing – review & editing, Investigation. **Joseph P. Heremans:** Writing – review & editing, Investigation, Funding acquisition. **Jagadeesh S. Moodera:** Writing – review & editing, Investigation, Funding acquisition. **Hang Chi:** Writing – original draft, Visualization, Investigation, Funding acquisition, Conceptualization.

Declaration of competing interest

The authors declare that they have no known competing financial interests or personal relationships that could have appeared to influence the work reported in this paper.

Data availability

Data will be made available on request.

Acknowledgements

The work at the Army Research Laboratory was supported by a LUCI fellowship awarded by the Office of the Undersecretary of Defense/Basic Research Office. The work at OSU was supported by the Army Research Office (W911NF-21-2-0089). The work at MIT was supported by Army Research Office (W911NF-20-2-0061), National Science Foundation (NSF-DMR 1700137 and CIQM NSF-DMR 1231319) and Office of Naval Research (N00014-20-1-2306). H.C. was sponsored by the Army Research Laboratory under Cooperative Agreement Number W911NF-19-2-0015 and acknowledges the support of the Canada Research Chairs (CRC) Program and the Natural Sciences and Engineering Research Council of Canada (NSERC), Discovery Grant RGPIN-2024-06497.

Appendix A. Supplementary data

Supplementary data to this article can be found online at https://doi.org/10.1016/j.mtphys.2024.101486.

References

[1] H.J. Goldsmid, R.W. Douglas, The use of semiconductors in thermoelectric refrigeration, Brit. J. Appl. Phys 5 (1954) 386–390, https://doi.org/10.1088/0508-3443/5/11/303.

[2] F.D. Rosi, Thermoelectricity and thermoelectric power generation, Solid State Electron. 11 (1968) 833–868, https://doi.org/10.1016/0038-1101(68)90104-4.

[3] J.P. Heremans, B. Wiendlocha, in: C. Uher (Ed.), Chapter 2 Tetradymites: Bi_2Te_3-Related Materials in *Materials Aspect of Thermoelectricity*, CRC Press, 2016, pp. 39–93, https://doi.org/10.1201/9781315197029.

[4] B. Poudel, Q. Hao, Y. Ma, Y. Lan, A. Minnich, B. Yu, X. Yan, D. Wang, A. Muto, D. Vashaee, X. Chen, J. Liu, M.S. Dresselhaus, G. Chen, Z. Ren, High-thermoelectric performance of nanostructured bismuth antimony telluride bulk alloys, Science 320 (2008) 634–638, https://doi.org/10.1126/science.1156446.

[5] S.I. Kim, K.H. Lee, H.A. Mun, H.S. Kim, S.W. Hwang, J.W. Roh, D.J. Yang, W. H. Shin, X.S. Li, Y.H. Lee, G.J. Snyder, S.W. Kim, Dense dislocation arrays embedded in grain boundaries for high-performance bulk thermoelectrics, Science 348 (2015) 109–114, https://doi.org/10.1126/science.aaa4166.

[6] R. Deng, X. Su, Z. Zheng, W. Liu, Y. Yan, Q. Zhang, V.P. Dravid, C. Uher, M. G. Kanatzidis, X. Tang, Thermal conductivity in $Bi_{0.5}Sb_{1.5}Te_{3+x}$ and the role of dense dislocation arrays at grain boundaries, Sci. Adv. 4 (2018): eaar5606, https://doi.org/10.1126/sciadv.aar5606.

[7] J. He, T.M. Tritt, Advances in thermoelectric materials research: looking back and moving forward, Science 357 (2017): eaak9997, https://doi.org/10.1126/science.aak9997.

[8] J.P. Heremans, R.J. Cava, N. Samarth, Tetradymites as thermoelectrics and topological insulators, Nat. Rev. Mater. 2 (2017): 17049, https://doi.org/10.1038/natrevmats.2017.49.

[9] L.D. Hicks, M.S. Dresselhaus, Effect of quantum-well structures on the thermoelectric figure of merit, Phys. Rev. B 47 (1993) 12727–12731, https://doi.org/10.1103/PhysRevB.47.12727.

[10] L.D. Hicks, M.S. Dresselhaus, Thermoelectric figure of merit of a one-dimensional conductor, Phys. Rev. B 47 (1993) 16631–16634, https://doi.org/10.1103/PhysRevB.47.16631.

[11] J.P. Heremans, M.S. Dresselhaus, L.E. Bell, D.T. Morelli, When thermoelectrics reached the nanoscale, Nat. Nanotechnol. 8 (2013) 471–473, https://doi.org/10.1038/nnano.2013.129.

[12] R. Venkatasubramanian, E. Siivola, T. Colpitts, B. O'Quinn, Thin-film thermoelectric devices with high room-temperature figures of merit, Nature 413 (2001) 597–602, https://doi.org/10.1038/35098012.

[13] T.C. Harman, P.J. Taylor, M.P. Walsh, B.E. LaForge, Quantum dot superlattice thermoelectric materials and devices, Science 297 (2002) 2229–2232, https://doi.org/10.1126/science.1072886.

[14] N. Peranio, M. Winkler, M. Dürrschnabel, J. König, O. Eibl, Assessing antisite defect and impurity concentrations in Bi_2Te_3 based thin films by high-accuracy chemical analysis, Adv. Funct. Mater. 23 (2013) 4969–4976, https://doi.org/10.1002/adfm.201300606.

[15] H. Zhang, C.-X. Liu, X.-L. Qi, X. Dai, Z. Fang, S.-C. Zhang, Topological insulators in Bi_2Se_3, Bi_2Te_3 and Sb_2Te_3 with a single Dirac cone on the surface, Nat. Phys. 5 (2009) 438–442, https://doi.org/10.1038/nphys1270.

[16] Y.L. Chen, J.G. Analytis, J.-H. Chu, Z.K. Liu, S.-K. Mo, X.L. Qi, H.J. Zhang, D.H. Lu, X. Dai, Z. Fang, S.C. Zhang, I.R. Fisher, Z. Hussain, Z.-X. Shen, Experimental realization of a three-dimensional topological insulator, Bi_2Te_3, Science 325 (2009) 178–181, https://doi.org/10.1126/science.1173034.

[17] Y. Xia, D. Qian, D. Hsieh, L. Wray, A. Pal, H. Lin, A. Bansil, D. Grauer, Y.S. Hor, R. J. Cava, M.Z. Hasan, Observation of a large-gap topological-insulator class with a single Dirac cone on the surface, Nat. Phys. 5 (2009) 398–402, https://doi.org/10.1038/nphys1274.

[18] D. Hsieh, Y. Xia, D. Qian, L. Wray, J.H. Dil, F. Meier, J. Osterwalder, L. Patthey, J. G. Checkelsky, N.P. Ong, A.V. Fedorov, H. Lin, A. Bansil, D. Grauer, Y.S. Hor, R. J. Cava, M.Z. Hasan, A tunable topological insulator in the spin helical Dirac transport regime, Nature 460 (2009) 1101–1105, https://doi.org/10.1038/nature08234.

[19] M.Z. Hasan, C.L. Kane, Colloquium: topological insulators, Rev. Mod. Phys. 82 (2010) 3045–3067, https://doi.org/10.1103/RevModPhys.82.3045.

[20] X.-L. Qi, S.-C. Zhang, Topological insulators and superconductors, Rev. Mod. Phys. 83 (2011) 1057–1110, https://doi.org/10.1103/RevModPhys.83.1057.

[21] A. Bansil, H. Lin, T. Das, Colloquium: topological band theory, Rev. Mod. Phys. 88 (2016): 021004, https://doi.org/10.1103/RevModPhys.88.021004.

[22] X.-G. Wen, Colloquium: zoo of quantum-topological phases of matter, Rev. Mod. Phys. 89 (2017): 041004, https://doi.org/10.1103/RevModPhys.89.041004.

[23] N.P. Armitage, E.J. Mele, A. Vishwanath, Weyl and Dirac semimetals in three-dimensional solids, Rev. Mod. Phys. 90 (2018): 015001, https://doi.org/10.1103/RevModPhys.90.015001.

[24] B.Q. Lv, T. Qian, H. Ding, Experimental perspective on three-dimensional topological semimetals, Rev. Mod. Phys. 93 (2021): 025002, https://doi.org/10.1103/RevModPhys.93.025002.

[25] C.-Z. Chang, C.-X. Liu, A.H. MacDonald, Colloquium: quantum anomalous Hall effect, Rev. Mod. Phys. 95 (2023): 011002, https://doi.org/10.1103/RevModPhys.95.011002.

[26] C.-Z. Chang, J. Zhang, X. Feng, J. Shen, Z. Zhang, M. Guo, K. Li, Y. Ou, P. Wei, L.-L. Wang, Z.-Q. Ji, Y. Feng, S. Ji, X. Chen, J. Jia, X. Dai, Z. Fang, S.-C. Zhang, K. He, Y. Wang, L. Lu, X.-C. Ma, Q.-K. Xue, Experimental observation of the quantum anomalous Hall effect in a magnetic topological insulator, Science 340 (2013) 167–170, https://doi.org/10.1126/science.1234414.

[27] C.-Z. Chang, W. Zhao, D.Y. Kim, H. Zhang, B.A. Assaf, D. Heiman, S.-C. Zhang, C. Liu, M.H.W. Chan, J.S. Moodera, High-precision realization of robust quantum anomalous Hall state in a hard ferromagnetic topological insulator, Nat. Mater. 14 (2015) 473–477, https://doi.org/10.1038/nmat4204.

[28] Y.-F. Zhao, R. Zhang, R. Mei, L.-J. Zhou, H. Yi, Y.-Q. Zhang, J. Yu, R. Xiao, K. Wang, N. Samarth, M.H.W. Chan, C.-X. Liu, C.-Z. Chang, Tuning the Chern number in quantum anomalous Hall insulators, Nature 588 (2020) 419–423, https://doi.org/10.1038/s41586-020-3020-3.

[29] P. Wei, F. Katmis, B.A. Assaf, H. Steinberg, P. Jarillo-Herrero, D. Heiman, J. S. Moodera, Exchange-coupling-Induced symmetry breaking in topological insulators, Phys. Rev. Lett. 110 (2013): 186807, https://doi.org/10.1103/PhysRevLett.110.186807.

[30] F. Katmis, V. Lauter, F.S. Nogueira, B.A. Assaf, M.E. Jamer, P. Wei, B. Satpati, J. W. Freeland, I. Eremin, D. Heiman, P. Jarillo-Herrero, J.S. Moodera, A high-temperature ferromagnetic topological insulating phase by proximity coupling, Nature 533 (2016) 513–516, https://doi.org/10.1038/nature17635.

[31] H. Chi, J.S. Moodera, Progress and prospects in the quantum anomalous Hall effect, APL. Mater. 10 (2022): 090903, https://doi.org/10.1063/5.0100989.

[32] H. Chi, W. Liu, C. Uher, Chapter 3 Growth and Transport Properties of Tetradymite Thin Films in *Materials Aspect of Thermoelectricity*, CRC Press, 2016, pp. 95–124, https://doi.org/10.1201/9781315197029.

[33] C.M. Jaworski, V. Kulbachinskii, J.P. Heremans, Resonant level formed by tin in Bi_2Te_3 and the enhancement of room-temperature thermoelectric power, Phys. Rev. B 80 (2009): 233201, https://doi.org/10.1103/PhysRevB.80.233201.

[34] H. Chi, W. Liu, K. Sun, X. Su, G. Wang, P. Lošťák, V. Kucek, Č. Drašar, C. Uher, Low-temperature transport properties of Tl-doped Bi_2Te_3 single crystals, Phys. Rev. B 88 (2013): 045202, https://doi.org/10.1103/PhysRevB.88.045202.

[35] S. Ishiwata, Y. Shiomi, J.S. Lee, M.S. Bahramy, T. Suzuki, M. Uchida, R. Arita, Y. Taguchi, Y. Tokura, Extremely high electron mobility in a phonon-glass semimetal, Nat. Mater. 12 (2013) 512–517, https://doi.org/10.1038/nmat3621.

[36] H. Chi, G. Tan, M.G. Kanatzidis, Q. Li, C. Uher, A low-temperature study of manganese-induced ferromagnetism and valence band convergence in tin telluride, Appl. Phys. Lett. 108 (2016): 182101, https://doi.org/10.1063/1.4948523.

[37] H. Chi, C. Zhang, G. Gu, D.E. Kharzeev, X. Dai, Q. Li, Lifshitz transition mediated electronic transport anomaly in bulk $ZrTe_5$, New J. Phys. 19 (2017): 015005, https://doi.org/10.1088/1367-2630/aa55a3.

[38] A.A. Abrikosov, Quantum magnetoresistance, Phys. Rev. B 58 (1998) 2788–2794. http://link.aps.org/doi/10.1103/PhysRevB.58.2788.

[39] J. Hu, T.F. Rosenbaum, Classical and quantum routes to linear magnetoresistance, Nat. Mater. 7 (2008) 697–700, https://doi.org/10.1038/nmat2259.

[40] X. Wang, Y. Du, S. Dou, C. Zhang, Room temperature giant and linear magnetoresistance in topological insulator Bi_2Te_3 nanosheets, Phys. Rev. Lett. 108 (2012): 266806, https://doi.org/10.1103/PhysRevLett.108.266806.

[41] T. Liang, Q. Gibson, M.N. Ali, M. Liu, R.J. Cava, N.P. Ong, Ultrahigh mobility and giant magnetoresistance in the Dirac semimetal Cd_3As_2, Nat. Mater. 14 (2015) 280–284, https://doi.org/10.1038/nmat4143.

[42] D. Shoenberg, Magnetic Oscillations in Metals, Cambridge University Press, Cambridge, 1984, https://doi.org/10.1017/CBO9780511897870.

[43] D.-X. Qu, Y.S. Hor, J. Xiong, R.J. Cava, N.P. Ong, Quantum oscillations and Hall anomaly of surface states in the topological insulator Bi_2Te_3, Science 329 (2010) 821–824, https://doi.org/10.1126/science.1189792.

[44] W. Zhao, X. Wang, Berry phase in quantum oscillations of topological materials, Adv. Phys. X 7 (2022): 2064230, https://doi.org/10.1080/23746149.2022.2064230.

[45] M. Ben Shalom, A. Ron, A. Palevski, Y. Dagan, Shubnikov-de Haas oscillations in $SrTiO_3/LaAlO_3$ interface, Phys. Rev. Lett. 105 (2010): 206401, https://doi.org/10.1103/PhysRevLett.105.206401.

[46] Y.-B. Gao, B. He, D. Parker, I. Androulakis, J.P. Heremans, Experimental study of the valence band of Bi_2Se_3, Phys. Rev. B 90 (2014): 125204, https://doi.org/10.1103/PhysRevB.90.125204.

[47] W. Zhao, L. Chen, Z. Yue, Z. Li, D. Cortie, M. Fuhrer, X. Wang, Quantum oscillations of robust topological surface states up to 50 K in thick bulk-insulating topological insulator, npj Quantum Mater. 4 (2019) 56, https://doi.org/10.1038/s41535-019-0195-7.

[48] W. Zhao, C.X. Trang, Q. Li, L. Chen, Z. Yue, A. Bake, C. Tan, L. Wang, M. Nancarrow, M. Edmonds, D. Cortie, X. Wang, Massive Dirac fermions and strong Shubnikov-de Haas oscillations in single crystals of the topological insulator Bi_2Se_3 doped with Sm and Fe, Phys. Rev. B 104 (2021): 085153, https://doi.org/10.1103/PhysRevB.104.085153.

[49] L. Zhang, T. Helm, H. Lin, F. Fan, C. Le, Y. Sun, A. Markou, C. Felser, Quantum oscillations in ferromagnetic $(Sb, V)_2Te_3$ topological insulator thin films, Adv. Mater. 33 (2021): 2102107, https://doi.org/10.1002/adma.202102107.

[50] X. Tang, Z. Li, W. Liu, Q. Zhang, C. Uher, A comprehensive review on Bi_2Te_3-based thin films: thermoelectrics and beyond, Interdisp. Mater. 1 (2022) 88–115, https://doi.org/10.1002/idm2.12009.

[51] Q.L. He, T.L. Hughes, N.P. Armitage, Y. Tokura, K.L. Wang, Topological spintronics and magnetoelectronics, Nat. Mater. 21 (2022) 15–23, https://doi.org/10.1038/s41563-021-01138-5.